



# Nanocomposite $\text{LaFe}_{1-x}\text{Ni}_x\text{O}_3$ /Palygorskite catalyst for photo-assisted reduction of $\text{NO}_x$ : Effect of Ni doping

Xiazhang Li<sup>a</sup>, Haiyang Shi<sup>a</sup>, Wei Zhu<sup>a</sup>, Shixiang Zuo<sup>a</sup>, Xiaowang Lu<sup>a</sup>, Shiping Luo<sup>a</sup>, Zhongyu Li<sup>a</sup>, Chao Yao<sup>a,\*</sup>, Yongsheng Chen<sup>b,\*</sup>

<sup>a</sup> Advanced Catalysis and Green Manufacturing Collaborative Innovation Center, Changzhou University, Changzhou 213164, PR China

<sup>b</sup> School of Civil and Environmental Engineering, Georgia Institute of Technology, Atlanta, GA 30332-0373, USA

## ARTICLE INFO

### Keywords:

Photo-SCR  
Palygorskite  
Perovskite  
Low-temperature  
 $\text{NO}_x$  Reduction

## ABSTRACT

Nitrogen oxide ( $\text{NO}_x$ ) is one of the world's major air pollutants. Thus, utilizing inexpensive mineral materials to develop an efficient and low-temperature denitrification catalyst is of great significance. In the present work, palygorskite (Pal)-supported perovskite-type  $\text{LaFe}_{1-x}\text{Ni}_x\text{O}_3$  ( $x = 0.1\text{--}0.9$ ) nanocomposites are prepared by a facile sol-gel method. Extensive tests are employed to characterize the textural and structural properties of samples. It is determined that perovskite particles are well dispersed on the surface of Pal with excellent  $\text{NH}_3$  adsorption. The impacts of various Ni doping on the  $\text{NO}_x$  conversion under visible light irradiation are investigated. Results indicate that when  $x$  is less than 0.4,  $\text{LaFe}_{1-x}\text{Ni}_x\text{O}_3$  remains a perovskite solid solution supported uniformly on the Pal surface. When  $x$  is beyond 0.4,  $\text{LaNiO}_3$  phase co-precipitates and forms a coherent heterojunction of  $\text{LaNiO}_3/\text{LaFe}_{0.6}\text{Ni}_{0.4}\text{O}_3$  on Pal. Photo-assisted selected catalytic reduction (Photo-SCR) of NO results show that the denitrification performance varies with the Ni content, and more than 90% of NO molecules can be reduced when  $x = 0.5$  in low temperature range of 150–250 °C.

## 1. Introduction

Nitrogen oxides ( $\text{NO}_x$ ) such as nitric oxide (NO), nitrogen dioxide ( $\text{NO}_2$ ), and nitrous oxide ( $\text{N}_2\text{O}$ ) are emitted from the power plants and motor vehicles [1,2], causing acid rain, which is harmful to the ecosystem [3]. Selective catalytic reduction (SCR) with ammonia has been widely implemented for removal of  $\text{NO}_x$  emissions [4]. A variety of  $\text{NH}_3$ -SCR catalysts have been developed to deal with the main pollutants from mobile emission resources, such as metal oxides [5], precious metals [6], mixed metal oxides [7] and perovskite oxides [8–10]. The commercialized industrial  $\text{NH}_3$ -SCR catalysts for stationary emission resources mainly include  $\text{WO}_3\text{--V}_2\text{O}_5/\text{TiO}_2$  and  $\text{MoO}_3\text{--V}_2\text{O}_5/\text{TiO}_2$ . However, they are only active within a narrow temperature range of 300 °C–400 °C and are normally installed prior to particulate removal to avoid reheating of the flue gas, which makes these catalysts susceptible to deactivation from sulfur and dust. Thus, a lot of efforts have been made to develop alternative techniques and provide new catalysts for operating SCR at low temperatures.

Photo-assisted selective catalytic reduction (Photo-SCR) of  $\text{NO}_x$  with ammonia ( $\text{NH}_3$ ), which can work at low temperature and reduce energy consumption, has been proposed at this stage [10,11]. Titanium dioxide ( $\text{TiO}_2$ ) and dye-sensitized  $\text{TiO}_2$  have been reported as photo-SCR

catalysts that can function at low temperature [12]. However, the insufficient utilization rate of visible light, and the easy recombination of electrons and holes greatly limits its application. Therefore, it is imperative that researchers develop a new catalyst, which can solve these problems. Recently, perovskite described by the general formula  $\text{ABO}_3$  has attracted much attention in the photocatalytic areas, since some of them possess narrow band gap meaning they have considerable visible light response. Thirumalairajan et al. [13] reported  $\text{LaFeO}_3$  exhibited higher photoactivity than  $\text{TiO}_2$  in the degradation of Rhodamine B under visible light irradiation, Qu et al. [14] prepared nanostructured materials of nickel titanate ( $\text{NiTiO}_3$ ) and Tang et al. [15] prepared multiferroic perovskite ( $\text{YFeO}_3$ ), which exhibited similar photodegradation for rhodamine B (RhB). Generally, in a perovskite structure, the A cation can be a lanthanide, alkaline, or alkaline-earth cations, while the B cation is a metallic element from a 3d, 4d, or 5d configuration. An A or B site is easily replaced or doped by other elements, which makes the structure of perovskite flexibly tunable. Previous studies on perovskites with respect to  $\text{NO}_x$  reduction suggest the possibility of replacing platinum-group metals with perovskite in the catalytic conversion of automotive exhaust [16]. To date, perovskites have indeed been considered as alternatives in various catalytic applications, mainly due to their synthetic flexibility and low cost compared

\* Corresponding authors.

E-mail addresses: [yaochao@cczu.edu.cn](mailto:yaochao@cczu.edu.cn) (C. Yao), [yongsheng.chen@ce.gatech.edu](mailto:yongsheng.chen@ce.gatech.edu) (Y. Chen).

to noble metals, and the extraordinary capability of their structure to accommodate a wide range of substituting and doping elements, which allows their properties to be tailored for better targeting of the desired applications [17]. However, pure perovskite catalysts have many drawbacks such as uncontrollable particle size, easy agglomeration and weak recyclability. Their enhancement is of crucial importance to the performance of the catalysts via modification upon their dispersion from active sites and the interaction of metal-support [18]. It is well known that a variety of supporting materials have been used such as a molecular sieve [19], graphene [20] and  $\text{TiO}_2$  [21], however, they have limitations in terms of their microporous structure and their surface active groups. Thus, it is necessary to immobilize perovskite particles on an appropriate matrix. Clay materials have been widely considered to be the most promising supporting material for solving these problems [22].

Palygorskite (Pal) is a natural hydrated magnesium aluminum silicate owning 1-D fibrous morphology with a diameter in nanometers [23]. Because of its low cost and large specific surface, Pal has been considered to be an ideal natural catalyst support. We previously reported that  $\text{La}_{1-x}\text{Ce}_x\text{MnO}_3/\text{Pal}$  catalysts had been prepared by a sol-gel method with citric acid [24], which exhibited higher activity than that pure  $\text{La}_{1-x}\text{Ce}_x\text{MnO}_3$  and Pal for  $\text{NH}_3$ -SCR improvement when working with  $\text{NO}_x$  at low temperature. To the best of our knowledge, there has been no report of a Pal-supported perovskite catalyst for  $\text{deNO}_x$  for photo-SCR strategy. Therefore, in this work, our first goal was to load perovskite  $\text{LaFeO}_3$  on the Pal surface via a facile sol-gel method. The  $\text{LaFe}_{1-x}\text{Ni}_x\text{O}_3/\text{Pal}$  nanocomposite with various Ni doping was expected to demonstrate an excellent visible light response range and reduced recombination probability of electrons and holes due to the rational formation of a “solid solution/co-precipitation heterostructure” [25]. The composition-activity on the photo-SCR removal of  $\text{NO}_x$  was investigated with various molar fractions of Ni to elucidate the mechanisms that determine photo-SCR activity. This work is expected to open new opportunities toward further development of new catalysts with excellent potential for industrial denitration.

## 2. Experimental

### 2.1. Chemicals

$\text{La}(\text{NO}_3)_3 \cdot 6\text{H}_2\text{O}$ ,  $\text{C}_6\text{H}_8\text{O}_7 \cdot \text{H}_2\text{O}$ ,  $\text{Ni}(\text{NO}_3)_2 \cdot 6\text{H}_2\text{O}$ ,  $\text{Fe}(\text{NO}_3)_3 \cdot 9\text{H}_2\text{O}$  were provided by Sinopharm Chemical Reagent Co., Ltd. Pal was provided by the Jiangsu Nanda Zijin Technology Group Co., Ltd. (Changzhou, China). Citric acid and ethylene glycol were purchased from the Shanghai Ling Feng Chemical Reagent Co., Ltd., China. All reagents were of analytical grade and used without further purification.

### 2.2. Synthesis of $\text{LaFe}_{1-x}\text{Ni}_x\text{O}_3/\text{Pal}$

All the reagents were of analytical grade and used without further purification.  $\text{LaFe}_{1-x}\text{Ni}_x\text{O}_3/\text{Pal}$  nanocomposites were prepared by the facile sol-gel method. 1.34 g of lanthanum nitrate, 0.12 g of nickel nitrate, 1.50 g of ferric nitrate and 1.80 g citric acid were mixed in a 250 ml beaker when  $x = 0.1$ . The amount of nitrate changed when the  $x$  was different. To this mixture, 10 ml of deionized water was added under ultrasonic dissolving. The molar ratio of Fe: Ni =  $x$  (0.1–0.9). The mixed solution was maintained at  $80^\circ\text{C}$  under stirring for one hour, followed by the addition of 1 g Pal. The composite catalyst was obtained after calcined at  $650^\circ\text{C}$  for 2 h.

### 2.3. Characterization

The TEM images were obtained using a transmission electron microscope (JEM-2100, JEOL, Japan), working at 200 kV. The XRD patterns were captured using an X-ray Rigaku D/Max-2500 diffractometer equipped with a Cu anode (Rigaku Corporation, Tokyo, Japan), running

at 60 kV and 30 mA with  $2\theta$  range between  $10^\circ$  and  $80^\circ$  at a scan rate of  $0.05^\circ$  per second. Raman spectra were measured at room temperature by a Thermo Fisher Scientific DXR Raman spectrophotometer, and the excitation laser wave length was 532 nm using a laser power level of about 5 mW. The Fourier transform infrared spectrum was measured using a PerkinElmer Spectrum 100 FT-IR spectrometer (PerkinElmer, Shelton, CT, USA). The UV-vis diffuse reflectance spectra (DRS) of catalysts were recorded on a UV-2700 spectrometer (Shimadzu, Japan) equipped with an integrating sphere using  $\text{BaSO}_4$  as the reflectance sample. The active components of  $\text{LaFe}_{1-x}\text{Ni}_x\text{O}_3$  were determined to be 40 wt% compared with the Pal by calculation in the precursor amount. The total acidity and the acid distribution of the catalysts were performed by the temperature-programmed desorption (TPD) of  $\text{NH}_3$  on a Micrometrics ASAP 2920 instrument with a TCD detector (Micrometrics, USA). A 0.3 g sample (sieved to 0.2–0.3 mm) was inserted into a fixed-bed flow reactor using  $\text{N}_2$  as the flow gas. The samples were degassed at  $400^\circ\text{C}$  for 30 min and then cooled to room temperature. The introduction of  $\text{NH}_3$  was carried out over 30 min followed by a purge with  $\text{N}_2$  to remove the physically adsorbed  $\text{NH}_3$  on the catalyst surface. Desorption under  $\text{N}_2$  was then carried out at  $25$ – $500^\circ\text{C}$  with a heating rate of  $10^\circ\text{C}/\text{min}$ .  $\text{H}_2$ -TPR was performed on a Micrometrics ASAP 2920 instrument with the TCD detector (Micrometrics, USA). Samples of approximately 50 mg were heated from ambient temperature to  $700^\circ\text{C}$  at  $10^\circ\text{C}/\text{min}$  and a mixture of  $\text{H}_2$  (10 vol. %) and Ar was employed as a reducing atmosphere at a flow rate of 30 ml/min. X-ray photoelectron spectroscopy (XPS) measurements were carried out with a Quantum 2000 Scanning ESCA Microprobe instrument using Al-K $\alpha$ . The Cls signal was set to a position of 284.6 eV.

### 2.4. Photo-SCR performance

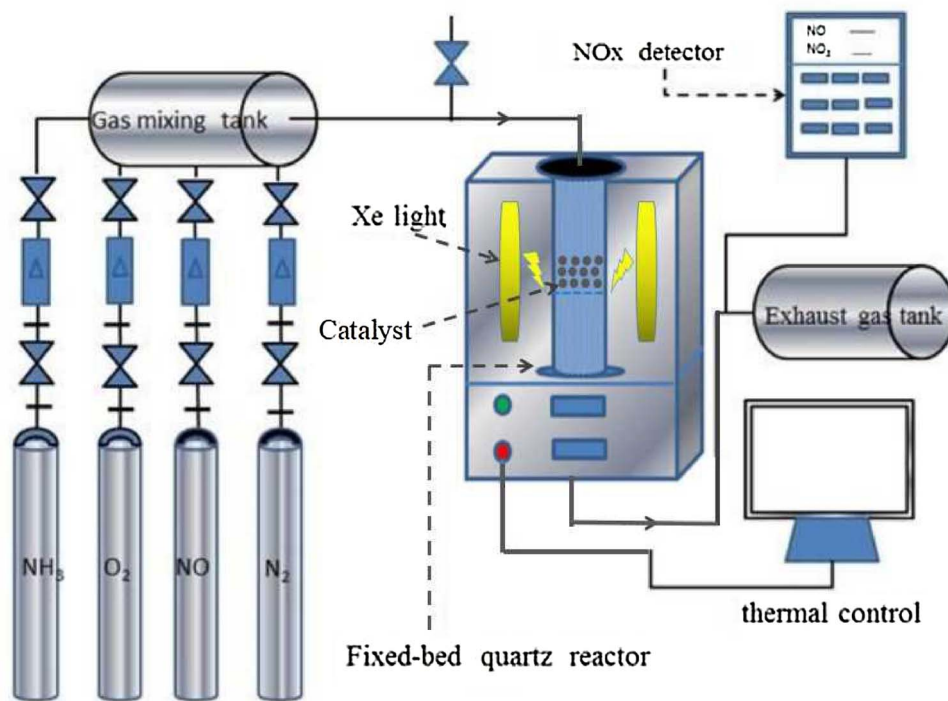
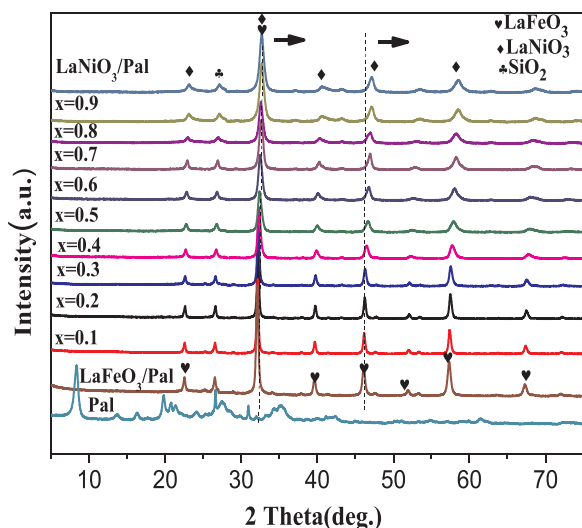
The photo-SCR catalytic experiments were carried out in a fixed-bed reactor operating in a steady state flow mode, and a 500W xenon lamp was employed as a simulated solar light source irradiation. The schematic diagram of the experiment was shown in Fig. 1. Two UV-filters were placed at both ends of the window to cut off the light with the wavelength lower than 420 nm to guarantee visible light irradiation. The reaction temperature was measured through a thermocouple projecting close to the surface of the catalyst. The reactant gas consisted of 1000 ppm NO, 1000 ppm  $\text{NH}_3$ , 3 vol. %  $\text{O}_2$  with balance in  $\text{N}_2$ , which is according to practical SCR conditions [26]. The catalyst was mixed with quartz sand (30–60 mesh) and deposited on a sieve plate located in the center of cylindrical quartz tube to ensure the penetration of the light as well as flow of the gas. The total flow rate was adjusted to 1 L/min by the mass flow control, corresponding to a GHSV (gas hourly space velocity) of  $40,000\text{ h}^{-1}$ . A flue gas analyzer (KM9106, Kane International Ltd.) was used to measure the inlet and outlet concentrations of  $\text{NO}_x$ . The concentrations of gas were measured by flue gas analyzer once every 5 min during the reaction. The main SCR reactions were described as follows [27]:

$$\text{NO}_x \text{ Conversion} = \frac{[\text{NO} + \text{NO}_2]_{\text{inlet}} - [\text{NO} + \text{NO}_2 + \text{N}_2\text{O}]_{\text{outlet}}}{[\text{NO} + \text{NO}_2]_{\text{inlet}}} \times 100\% \quad (1)$$

$$\text{N}_2 \text{ Selectivity} = 1 - \frac{[2\text{N}_2\text{O}]_{\text{outlet}}}{[\text{NO}_x]_{\text{inlet}} + [\text{NH}_3]_{\text{inlet}} - [\text{NO}_x]_{\text{outlet}} - [\text{NH}_3]_{\text{outlet}}} \times 100\% \quad (2)$$

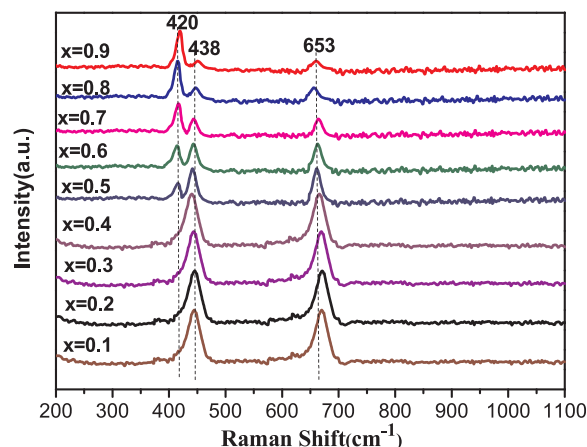
## 3. Results and discussion

Fig. 2 shows the XRD patterns of Pal and  $\text{LaFe}_{1-x}\text{Ni}_x\text{O}_3/\text{Pal}$  ( $x = 0$ –1). The XRD pattern of Pal clearly displays a typical reflection at  $8^\circ$ . The diffraction peak of Pal at  $26.6^\circ$  is ascribed to the impurity of quartz  $\text{SiO}_2$ . The typical diffraction peaks correspond to  $\text{LaFeO}_3$  (JCPDS

Fig. 1. The schematic diagram of photo-SCR of  $\text{NO}_x$ .Fig. 2. XRD patterns of various samples: Pal,  $\text{LaFeO}_3/\text{Pal}$ ,  $\text{LaNiO}_3/\text{Pal}$  and  $\text{LaFe}_{1-x}\text{Ni}_x\text{O}_3/\text{Pal}$  ( $x = 0-1$ ).

Card No.37-1493) and  $\text{LaNiO}_3$  (JCPDS Card No. 33-0711). For the  $\text{LaFe}_{1-x}\text{Ni}_x\text{O}_3/\text{Pal}$  samples, the diffraction peaks reveal a slight shift towards larger  $2\theta$  angles due to lattice contraction generated by substitution of Fe ion by Ni ion. In addition, the full-width at half-maximum of diffraction lines increases upon substitution of Fe ion by Ni ion. A new phase  $\text{LaNiO}_3$  appears when the doping content  $x$  is 0.5. These findings are in accordance with the general trend where the extent of nickel substitution is related to these effects and corresponds to some structure modification [28]. The peak shift towards higher  $2\theta$  angles as the nickel amount increases indicates a decrease in the interplanar distance.

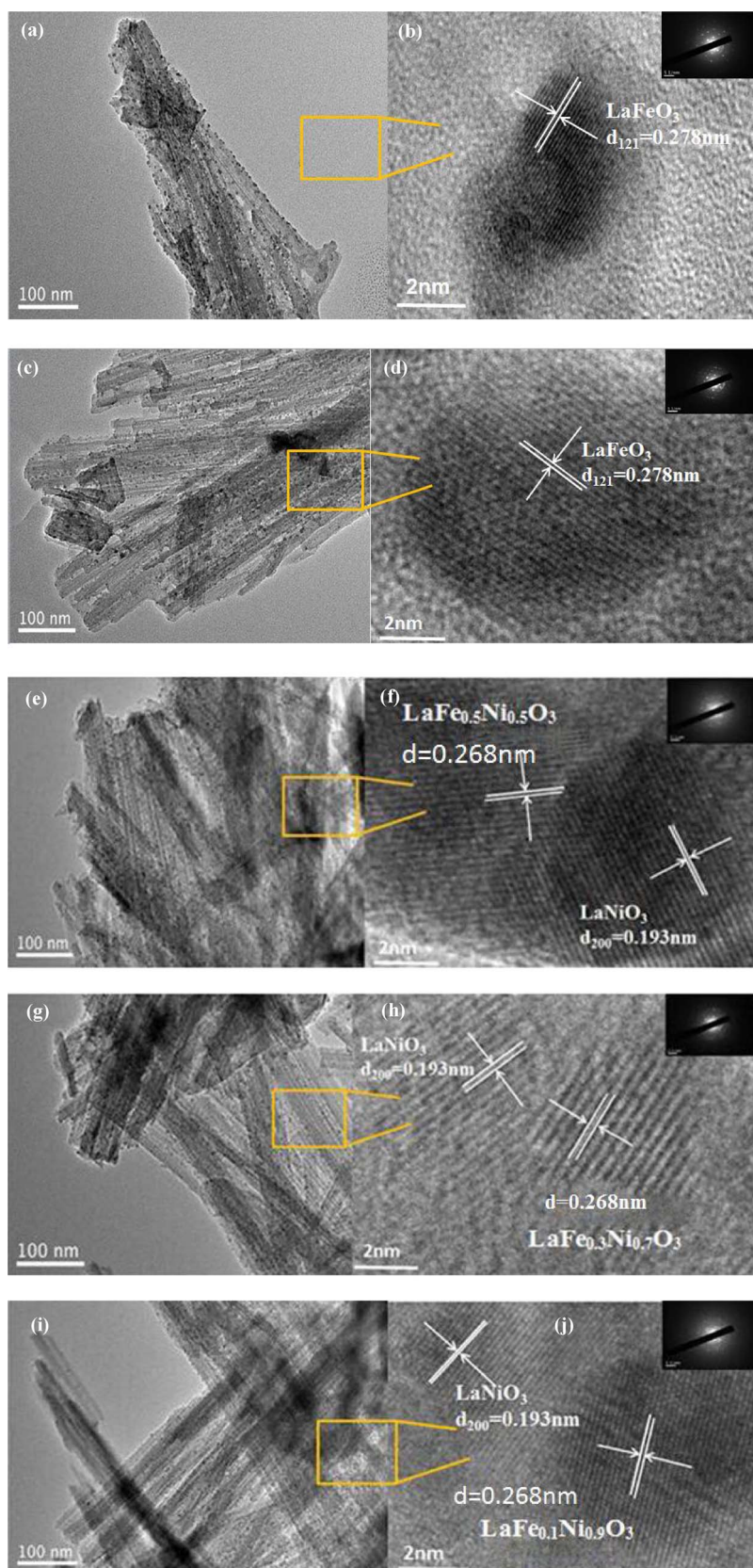
It is well known that Raman spectroscopy can be used to determine the structure distortion and oxygen motion of perovskite-type materials [29]. The main peaks of  $\text{LaFeO}_3$  were shown at approximately 438 and  $653\text{ cm}^{-1}$  (Fig. 3). With the increase of doping content of Ni, the band

Fig. 3. Raman spectra of  $\text{LaFe}_{1-x}\text{Ni}_x\text{O}_3/\text{Pal}$  ( $x$  from 0.1 to 0.9).

located at  $653\text{ cm}^{-1}$  decreased appreciably implying that the Ni ion might be incorporated into the  $\text{LaFeO}_3$  crystal structure, resulting the formation of  $\text{LaFe}_{1-x}\text{Ni}_x\text{O}_3$  solid solution with structure distortion [30]. When the doping content reaches 0.5, the characteristic peak of  $\text{LaNiO}_3$  showed up in  $420\text{ cm}^{-1}$  and increased progressively from 0.5 to 0.9, which was consistent with the XRD result.

The morphology of the  $\text{LaFe}_{1-x}\text{Ni}_x\text{O}_3/\text{Pal}$  was investigated by TEM (Fig. 4a-j). The perovskite-oxide particles with an average size of about 8 nm were loaded on the surface of Pal rods and were uniformly dispersed without obvious aggregation. Such a small size of perovskite particles may be due to the presence of abundant active sites on the Pal surface which may favor controlling the growth of perovskite grains. When the doping fraction  $x$  was less than 0.5, the lattice distance of  $0.278\text{ nm}$  was ascribed to  $\{121\}$  of  $\text{LaFeO}_3$ . However, when  $x$  was beyond 0.5, a new phase with a lattice distance of  $0.193\text{ nm}$  coexists, which corresponds to  $\{200\}$  of  $\text{LaNiO}_3$ , which are in agreement with the Raman results. The heterojunction of  $\text{LaNiO}_3/\text{LaFe}_{1-x}\text{Ni}_x\text{O}_3$  can be easily found in Fig. 4f, h and j. The SAED patterns showed that the structure of the crystal changed with different doping contents.





**Fig. 4.** Representative TEM and corresponding HRTEM images of  $\text{LaFe}_{1-x}\text{Ni}_x\text{O}_3/\text{Pal}$  nanocomposites (a and b)  $x = 0.1$ ; (c and d)  $x = 0.3$ ; (e and f)  $x = 0.5$ ; (g and h)  $x = 0.7$  and (i and j)  $x = 0.9$ .

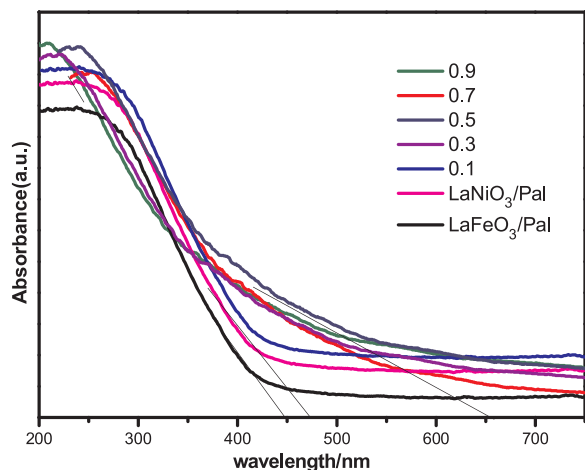


Fig. 5. UV-vis spectra of  $\text{LaFe}_{1-x}\text{Ni}_x\text{O}_3/\text{Pal}$  ( $x = 0, 0.1, 0.3, 0.5, 0.7, 0.9$  and  $1$ ).

The UV-vis absorption spectra of  $\text{LaFeO}_3/\text{Pal}$ ,  $\text{LaNiO}_3/\text{Pal}$  and  $\text{LaFe}_{1-x}\text{Ni}_x\text{O}_3/\text{Pal}$  with different doping amounts were shown in Fig. 5. Compared with the  $\text{LaFeO}_3/\text{Pal}$  and  $\text{LaNiO}_3/\text{Pal}$ , the  $\text{LaFe}_{1-x}\text{Ni}_x\text{O}_3/\text{Pal}$  enhanced absorption intensity in the visible region. The  $\text{LaFe}_{1-x}\text{Ni}_x\text{O}_3/\text{Pal}$  samples absorbed visible light with wavelengths more than 600 nm when  $x$  was from 0.1 to 0.9. This evolution of wavelength is due to the partial substitution of Fe with Ni forming impurity level [31,32]. When the doping content was 0.5, the sample presented an obvious red shift and the highest absorption edge up to 660 nm, due to the formation of a “solid solution/co-precipitation heterostructure” [25]. This phenomenon indicates that the Ni doping plays positive roles in light-harvesting from UV to visible range, and enabling photo-SCR under visible light which counts for a majority of the solar light.

X-ray photoelectron spectroscopy (XPS) was adopted to determine the composition of the  $\text{LaFe}_{1-x}\text{Ni}_x\text{O}_3/\text{Pal}$  nanocomposites. Fig. 6a displayed the representative survey spectrum of core levels for  $\text{LaFe}_{0.5}\text{Ni}_{0.5}\text{O}_3/\text{Pal}$  where La, Fe, Ni and O elements appeared. Fig. 6b showed both the superior width and asymmetry of the O1s XPS spectra,

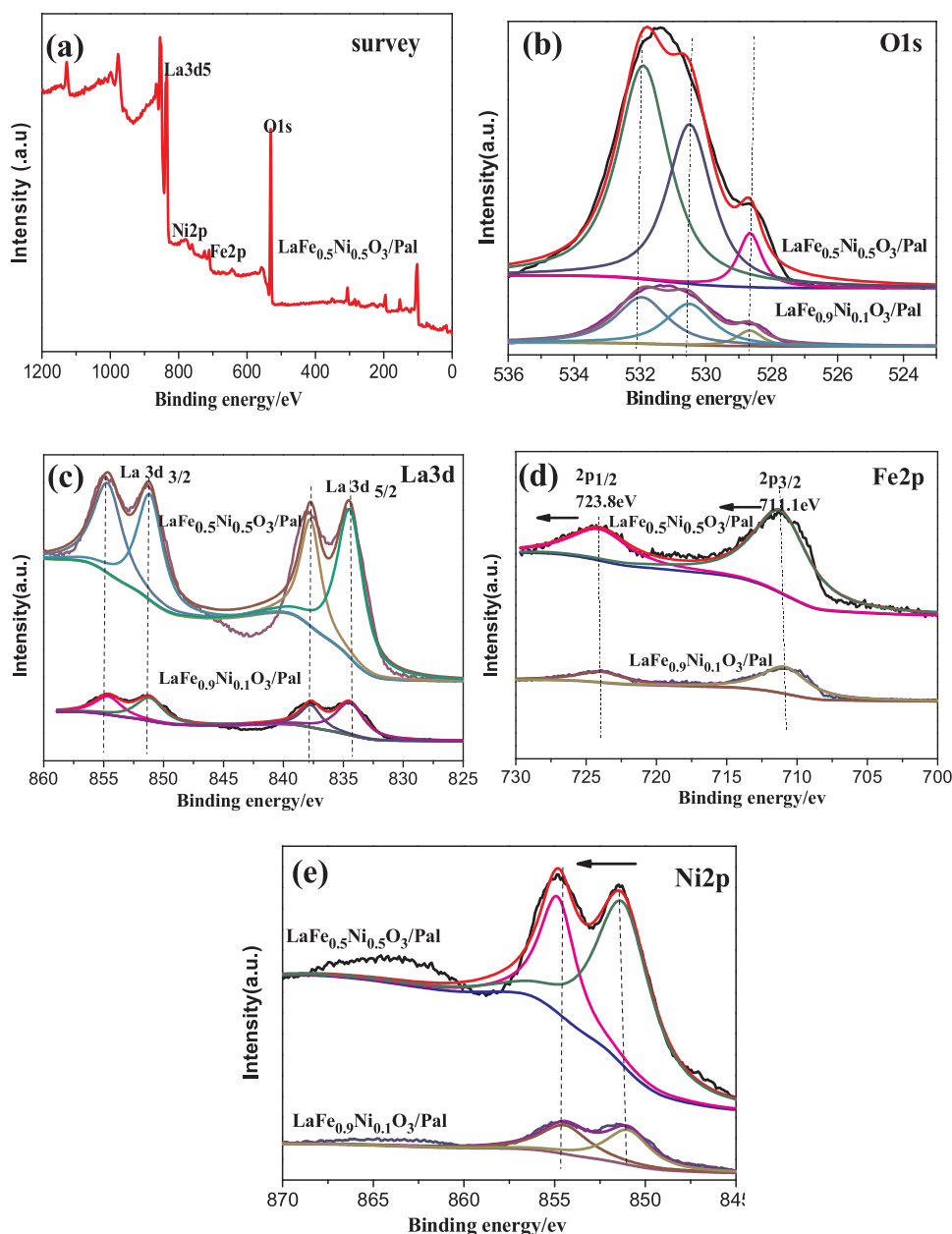


Fig. 6. XPS spectra of  $\text{LaFe}_{1-x}\text{Ni}_x\text{O}_3/\text{Pal}$  ( $x = 0.1$  and  $0.5$ ): (a) survey, (b) O 1s, (c) La 3d, (d) Fe 2p, and (e) Ni 2p.

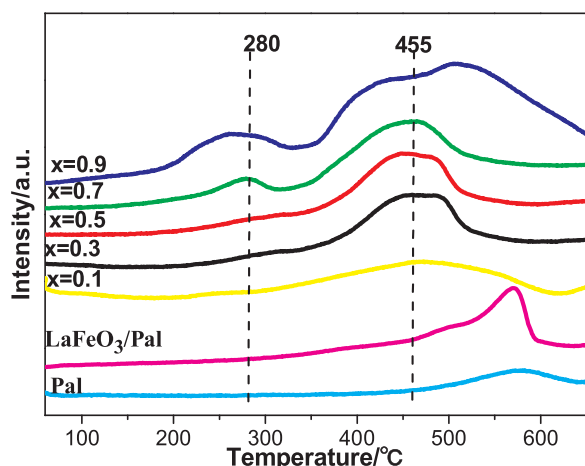


Fig. 7.  $H_2$ -TPR profiles of  $LaFe_{1-x}Ni_xO_3/Pal$  nanocomposites with various  $Ni^{3+}$  doping amounts.

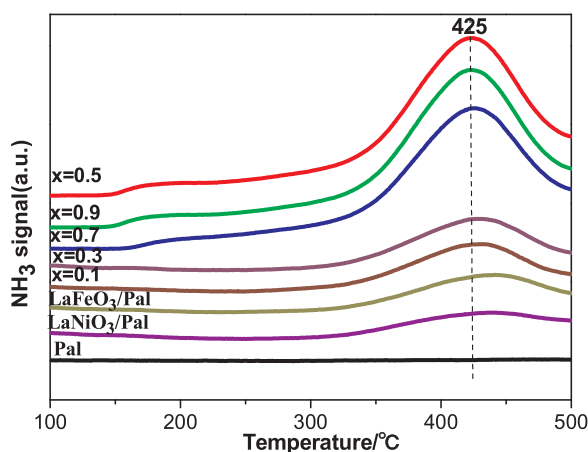


Fig. 8.  $NH_3$ -TPD profiles of  $LaFe_{1-x}Ni_xO_3/Pal$  nanocomposites with various Ni doping amounts.

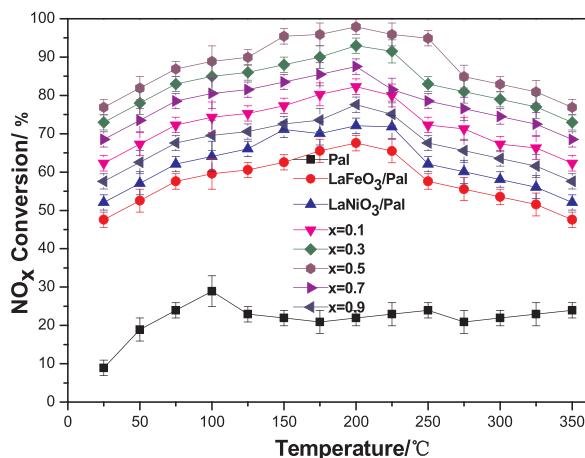


Fig. 9.  $NO_x$  conversion in photo-SCR with different samples.

demonstrating that there were several kinds of O chemical states according to the banding energy ranging from 528.0 to 534.0 eV, which were attributed to crystal lattice oxygen and adsorbed oxygen existed in the perovskite lattice [33,34]. Fig. 6c showed the main peak of La 3d5/2 at a binding energy of 835.7 eV attributed to the  $La^{3+}$  state, and it had little changes in terms of peak position due to the B site doping by similar radius ion normally had less effect as compared with A site in  $ABO_3$  type perovskite [35]. There appeared two peaks around 711.1 eV and 723.8 eV in Fig. 6d corresponding to Fe 2p 3/2 which was attributed to characteristic peaks of  $Fe^{3+}$  in composite, manifesting the presence of  $Fe^{3+}$  status both in  $LaFe_{0.9}Ni_{0.1}O_3/Pal$  and  $LaFe_{0.5}Ni_{0.5}O_3/Pal$  nanocomposites. It is worth mentioning that the peak intensity of  $LaFe_{0.5}Ni_{0.5}O_3/Pal$  was stronger than the counterpart of  $LaFe_{0.9}Ni_{0.1}O_3/Pal$  which may be associated with the enhance incorporation of Ni ion into perovskite structure. The spectrum of the Ni 2p was obtained at binding energy around 852 eV and 854 eV as shown in Fig. 6e. Compared to  $LaFe_{0.9}Ni_{0.1}O_3/Pal$  sample, the main peaks of Ni 2p in  $LaFe_{0.5}Ni_{0.5}O_3/Pal$  had an obviously shift to the higher binding energy, implying that the solid solution may reach saturation with the emergence of  $LaNiO_3$  phase, which was consistent with aforementioned TEM results.

Temperature-programmed reduction by  $H_2$  ( $H_2$ -TPR) is employed to reveal the influence of the Ni doping on the redox properties of catalysts (Fig. 7). The first peak appears at 280 °C indicating that the reduction of  $Ni^{3+}$  ions implies an oxygen loss from the structure [36]. The second peak with a maximum consumption of  $H_2$  at 455 °C leads to metallic nickel deposited on lanthanum oxide. As can be seen, Ni substitution hardly changes the redox properties with respect to  $LaFeO_3/Pal$ , despite an increase in  $H_2$  consumption of  $LaFe_{0.5}Ni_{0.5}O_3/Pal$ . Since the  $La^{3+}$  of perovskite can hardly be reverted to a lower valence state, the reduction of  $LaNiO_3$  here can be attributed to one step—namely  $Ni^{3+}$  to  $Ni^{2+}$  [37].

The  $NH_3$  adsorption property of catalyst is one of the significant factors in  $NH_3$ -SCR reaction.  $NH_3$ -TPD is carried out to investigate the amount of the surface acidic sites. According to the TPD result shown in Fig. 8, the pure Pal and  $LaFeO_3/Pal$  have no obvious peaks from 100 °C to 500 °C, suggesting a weak acid distribution site. However, the addition of Ni slightly increases the adsorption capability of  $NH_3$ , and the composite materials show a weak peak at 200 °C and a strong peak at 425 °C. When the content of Ni is increased to 0.5, it shows the highest amount of acidic sites. However, when the doping amount is beyond 0.5, the peak area gradually decreases, implying that the aggregation of  $LaNiO_3$  on the surface may be detrimental to the adsorption of  $NH_3$ .

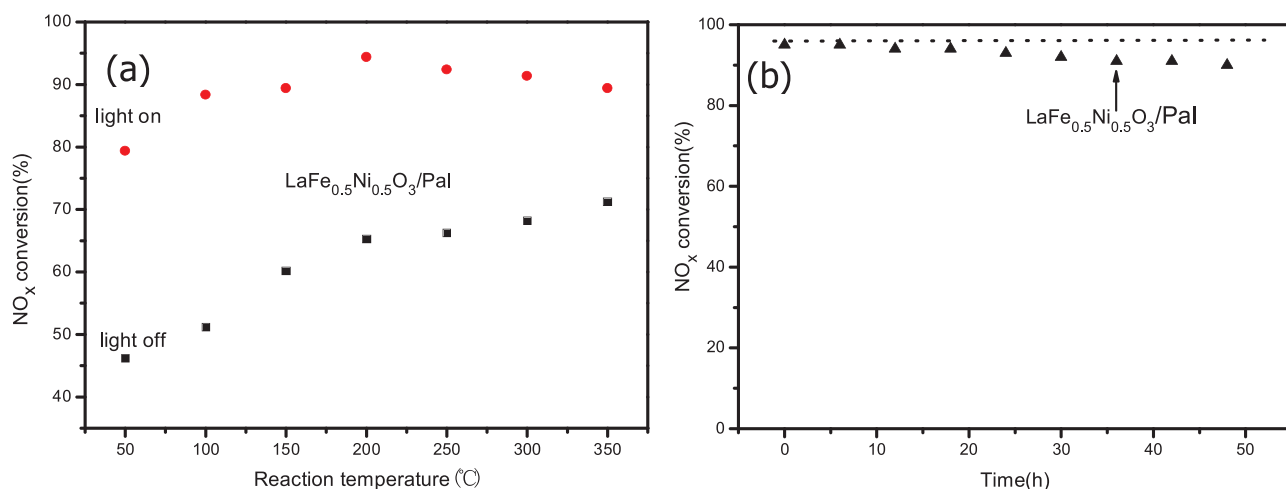
Fig. 9 showed  $NO_x$  conversion as a function of reaction temperatures between 25 °C and 350 °C over the Pal,  $LaFeO_3/Pal$ ,  $LaNiO_3/Pal$  and  $LaFe_{1-x}Ni_xO_3/Pal$  ( $x = 0.1, 0.3, 0.5, 0.7, 0.9$ ) catalysts. Each test of photo-SCR activity was carried out under triplicate experiments with the relative deviation generally less than 5%. The pure Pal exhibits very low  $NO_x$  conversion due to the limited adsorption ability of Pal. It is evident that the addition of Ni to  $LaFeO_3/Pal$  enhances the  $NO_x$  conversion greatly. When the doping content is 0.5, the  $NO_x$  conversion of the  $LaFe_{0.5}Ni_{0.5}O_3/Pal$  reaches 92%, which is the highest among these samples. It should be noted that  $LaFe_{0.5}Ni_{0.5}O_3/Pal$  sample did not possess the highest specific surface as shown in Table 1, however, the surface area was the highest when the Ni doping ratio was 0.6 consistent with Assaf et al.'s report [38], which demonstrated that the  $LaNi_{0.6}Fe_{0.4}O_3$  had much higher surface area than others performing the best catalysis activity for methane reforming. In order to identify

Table 1

Specific surface areas and reaction rates normalized by catalyst surface area ( $R_s$ ) at 200 °C over  $LaFe_{1-x}Ni_xO_3/Pal$ .

Doping ratio	0.1	0.2	0.3	0.4	0.5	0.6	0.7	0.8	0.9
Specific surface area/( $m^2/g$ )	45.23	50.34	48.56	50.72	60.54	76.70	45.66	50.43	39.15
RS at 200 °C ( $mmol\ s^{-1}\ m^{-2}$ )	0.037	0.041	0.045	0.051	0.062	0.048	0.046	0.038	0.033





**Fig. 10.** (a) The NO<sub>x</sub> conversion of LaFe<sub>0.5</sub>Ni<sub>0.5</sub>O<sub>3</sub>/Pal under the light on and light off with different reaction temperature and (b) the stability of LaFe<sub>1-x</sub>Ni<sub>x</sub>O<sub>3</sub>/Pal under different reaction times.

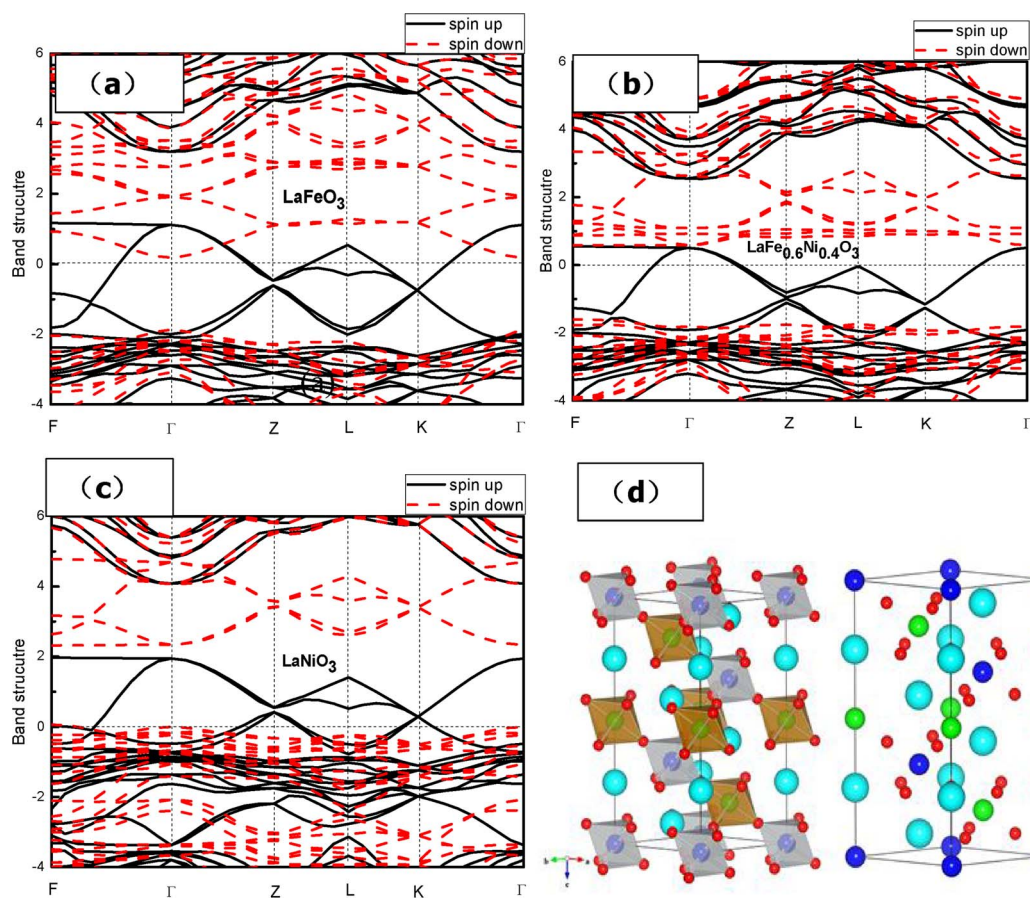


**Fig. 11.** DFT calculated electronic band structures of the LaFeO<sub>3</sub> (a), LaFe<sub>0.6</sub>Ni<sub>0.4</sub>O<sub>3</sub> solid solution (b), LaNiO<sub>3</sub> (c) and the cell structure of LaFe<sub>0.6</sub>Ni<sub>0.4</sub>O<sub>3</sub> solid solution (d) (the light blue ball corresponds to La atom, the dark blue ball corresponds to Ni atom, the green ball corresponds to Fe atom, the red ball corresponds to oxygen atom). (For interpretation of the references to colour in this figure legend, the reader is referred to the web version of this article.)

the intrinsic catalytic activity, the reaction rates of NO conversion normalized by the specific surface area ( $R_s$ ) are calculated by the following equation:  $R_s \text{ (mmol s}^{-1} \text{ m}^{-2}) = X_{\text{NO}} Q C_f / (W S_{\text{BET}})$ , where  $X_{\text{NO}}$  is the conversion rate of NO,  $Q$  is the volumetric flow rate (L/s) of simulated flue gas,  $C_f$  is the feed concentration (mmol/L) of NO,  $W$  is the weight of catalyst sample (g), and  $S_{\text{BET}}$  is the Brunauer–Emmett–Teller (BET) surface area of the catalyst ( $\text{m}^2/\text{g}$ ). The  $R_s$  increases with the increase of  $x$  from 0.1 to 0.5 while this trend reverses as  $x$  further increases to 0.9 which is not proportional to the changing of surface area,

implying that the photon associated capacity in the current work may play dominant role in the photo-SCR of NO.

To further evaluate the light effect on the photo-SCR of NO<sub>x</sub>, catalytic performance was carried out under light on and light off conditions at elevated temperature using LaFe<sub>0.5</sub>Ni<sub>0.5</sub>O<sub>3</sub>/Pal as catalyst. As shown in Fig. 10(a), compared to the SCR activity with the absence of visible light irradiation, photo-SCR had much lower reaction temperature and higher NO<sub>x</sub> conversion, suggesting that the as-prepared catalyst had enhanced low-temperature of deNO<sub>x</sub> due to the beneficial

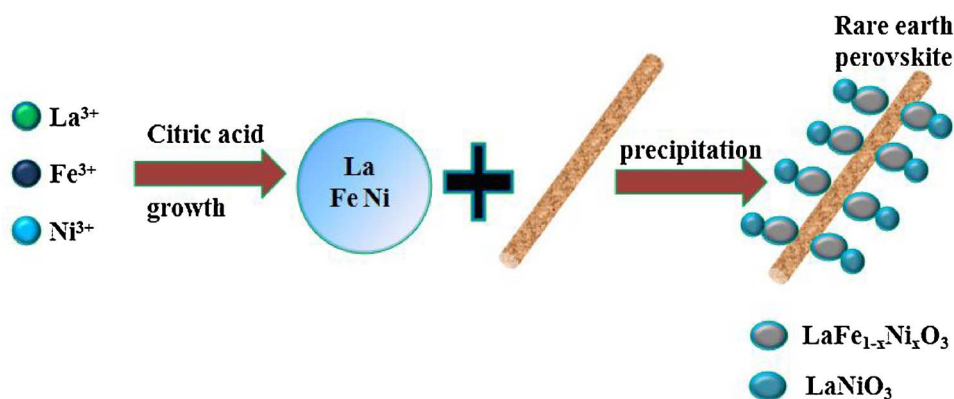


Fig. 12. Schematic of the formation of  $\text{LaFe}_{1-x}\text{Ni}_x\text{O}_3/\text{Pal}$  nanocomposite.

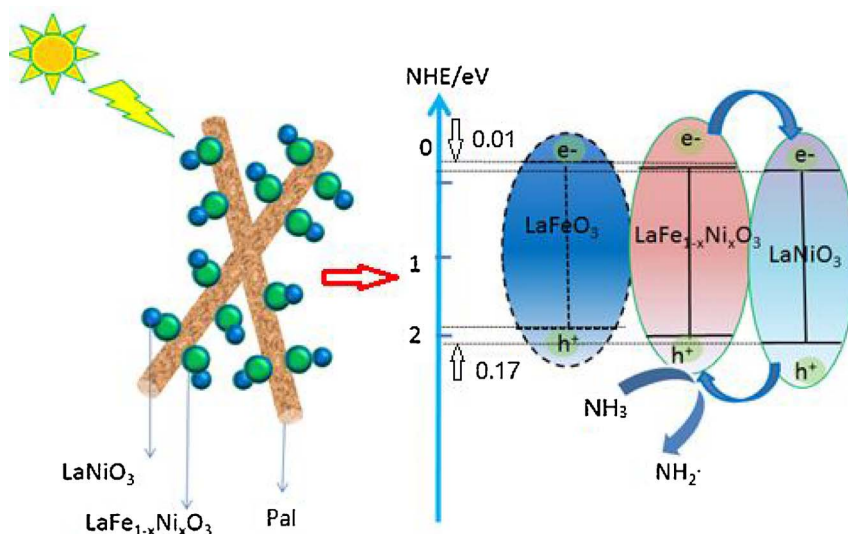


Fig. 13. Schematic illustration of photo-SCR mechanism for  $\text{LaFe}_{1-x}\text{Ni}_x\text{O}_3/\text{Pal}$ .

effect of optical effect beyond traditional SCR. When the temperature reached 200 °C, the  $\text{NO}_x$  conversion slightly decreased, which could be due to occurrence of electron-hole pair recombination at relatively high temperatures as reported by Westrich et al. [39]. In order to rule out the impact of photo-induced thermal effect, the light on-off cycle tests were conducted under visible light irradiation at room temperature shown in Fig. S1. It was found that the conversion of NO was about 18% without irradiation and the conversion rate reached 78% under irradiation, suggesting that the photocatalytic effect play important role in the photo-SCR reaction. The stability of  $\text{LaFe}_{0.5}\text{Ni}_{0.5}\text{O}_3/\text{Pal}$  at 200 °C was performed and shown in Fig. 10(b). The results indicated that the catalyst remained high  $\text{NO}_x$  conversion only with about 4.9% deactivation after 48h running, implying that the perovskite oxides immobilized on the Pal support may benefit the photo-stability [40].

The  $\text{N}_2$  selectivity curves of  $\text{LaFe}_{1-x}\text{Ni}_x\text{O}_3/\text{Pal}$  with various  $x$  doping were shown in Fig. S2.  $\text{N}_2$  selectivity of  $\text{LaFeO}_3/\text{Pal}$  and  $\text{LaNiO}_3/\text{Pal}$  reach 68% and 70% due to different photo responses and to the adsorption of Pal. When the doping content increases, the  $\text{N}_2$ -selectivity of the catalyst is higher than the pure  $\text{LaFeO}_3/\text{Pal}$  and  $\text{LaNiO}_3/\text{Pal}$ . When the doping amount is 0.5, the  $\text{N}_2$ -selectivity is 98%, which is the highest of all the as-prepared catalysts. It should be noted that  $\text{LaFe}_{0.5}\text{Ni}_{0.5}\text{O}_3/\text{Pal}$  can accommodate a high  $\text{N}_2$  selectivity when the reaction temperature is below 200 °C. However, the  $\text{N}_2$  selectivity decreases when the reaction temperature is above 200 °C due to the production of  $\text{N}_2\text{O}$  on the perovskite surface.

Generally, the separation efficiency of photogenerated electron-hole pairs is the key factor determining their photocatalytic activities, and

the matching energy band structure of the composite is the prerequisite, therefore we conducted DFT calculations to estimate the valence band (VB) offset and conductive band (CB) offset based on that the band gap of  $\text{LaFeO}_3$  and  $\text{LaNiO}_3$  were 2.10 eV and 2.26 eV respectively as revealed in Fig. 11. Due to the absence of nonpolar directions in the  $\text{LaFeO}_3$  and  $\text{LaNiO}_3$  material, we did not follow the standard super-lattice procedure in which the averaged electrostatic potentials were aligned by performing an interface calculation [41]. Alternatively, we determined the VB offset by measuring the energy difference between VB edges and O 2s orbitals, since O 2s orbitals served as benchmark are very deep and isolated in both cases and thus they could not be affected by Ni or Fe orbitals significantly. The exchange–correlation energy was described by the local spin density approximation. To account for the strong electron correlation of the Fe ions, all calculations were performed using the plus Hubbard U correction with  $U = 4$  eV. The results show that the energy difference between VB edge and O 2s orbitals are 18.22 and 18.05 eV in  $\text{LaFeO}_3$  and  $\text{LaNiO}_3$ , respectively, suggesting that the VB offset is 0.17 eV. Correspondingly, the CB offset between  $\text{LaFeO}_3$  and  $\text{LaNiO}_3$  is calculated to be 0.01 eV. It should be noted that after doping with Ni at  $x = 0.4$ , the CB and VB edge position of the solid solution  $\text{LaFe}_{0.6}\text{Ni}_{0.4}\text{O}_3$  is located between that of the original  $\text{LaFeO}_3$  and  $\text{LaNiO}_3$ , making the charge carriers' transports easier [42]. This obviously indicates that the introduction of Ni into  $\text{LaFeO}_3$  as a constituent element is an effective way for engineering the band edges of the valence band as well as the conduction band.

Fig. 12 showed the schematic formation of the  $\text{LaFe}_{1-x}\text{Ni}_x\text{O}_3/\text{Pal}$  nanocomposite. During the sol-gel process, the  $\text{La}^{3+}$ ,  $\text{Fe}^{3+}$  and  $\text{Ni}^{3+}$



ions form perovskite-type particles on the surface of Pal aided by citric complexation. When  $x$  was beyond 0.4,  $\text{LaNiO}_3$  phase co-precipitated and formed a coherent heterojunction of  $\text{LaNiO}_3/\text{LaFe}_{0.6}\text{Ni}_{0.4}\text{O}_3$  facilitated by the active  $-\text{OH}$  sites on Pal surface [22].

On the basis of the above experimental and calculation results, a mechanism for the photo-SCR of NO with  $\text{NH}_3$  by using  $\text{LaFe}_{1-x}\text{Ni}_x\text{O}_3/\text{Pal}$  is proposed as shown in Fig. 13. The mechanism is in accordance with previous findings by Tanaka's group [11]. Initially,  $\text{NH}_3$  is adsorbed on the Lewis acid site of  $\text{LaFe}_{1-x}\text{Ni}_x\text{O}_3$  in the dark facilitated by physisorption in the micropores of the Pal [24]. Adsorption of  $\text{NH}_3$  at the metal sites is followed by abstraction of one H-atom via interaction with the perovskite lattice oxygen leaving equal  $\text{NH}_2^-$  group. Next, under visible light irradiation, electrons derived from the N atoms of  $\text{NH}_3$  adsorbed on the catalyst transfer to  $\text{Fe}^{3+}$  and  $\text{Ni}^{3+}$  causing them to be reduced to  $\text{Fe}^{2+}$  and  $\text{Ni}^{2+}$  according to Tanaka group's report that the electron transfer takes place between adsorbent and adsorbed species [11]. The  $\text{LaFe}_{1-x}\text{Ni}_x\text{O}_3$  is excited to generate electrons ( $e^-$ ) and holes ( $h^+$ ) where electrons are quickly transferred to the coherent couple of the  $\text{LaNiO}_3$  surface. Simultaneously, the electrons are excited from the valance band of  $\text{LaNiO}_3$  to its conduction band, and both of those electrons are annihilated in the Pal framework as revealed in our previous work [43], leaving the holes in the valance band to transfer from  $\text{LaNiO}_3$  to  $\text{LaFe}_{1-x}\text{Ni}_x\text{O}_3$ . The charge separation effectively inhibits the recombination of the electrons and the holes. The photogenerated hole is captured by the  $\text{NH}_2^-$  evolved from the adsorbed  $\text{NH}_3$  to produce the  $\text{NH}_2$  radical. Then, NO in the gas phase is attacked by the  $\text{NH}_2$  radical and transformed to an  $\text{NH}_2\text{NO}$  intermediate. The  $\text{NH}_2\text{NO}$  intermediate is subsequently decomposes to  $\text{N}_2$  and  $\text{H}_2\text{O}$  as expressed in reference [44]. Finally, the  $\text{Fe}^{2+}$  and  $\text{Ni}^{2+}$  species are re-oxidized to  $\text{Fe}^{3+}$  and  $\text{Ni}^{3+}$  species by  $\text{O}_2$ . To examine consistency with the proposed mechanism, *in-situ* EPR measurements were performed and the results are shown in Fig. S3. Fig. S3(a) shows the EPR spectrum of  $\text{LaFe}_{0.5}\text{Ni}_{0.5}\text{O}_3/\text{Pal}$  after introduction of  $\text{NH}_3$  without irradiation in the dark and Fig. S3(b) shows the EPR spectrum of  $\text{LaFe}_{0.5}\text{Ni}_{0.5}\text{O}_3/\text{Pal}$  under irradiation. The EPR spectrum is centered around the single line of  $g = 2$  whereas the feature near  $g = 4.2$  is ascribed to  $\text{Fe}^{3+}(\text{Ni}^{3+})$  and becomes weaker in Fig. S3(b) suggesting the decrease of  $\text{Fe}^{3+}(\text{Ni}^{3+})$  [40]. New signals emerge at  $g = 2.006$ ,  $2.008$  and  $2.019$  in Fig. S3(b) attributable to the generation of the  $\text{NH}_2$  radical under photoirradiation [44].

#### 4. Conclusion

A series of nanocomposite  $\text{LaFe}_{1-x}\text{Ni}_x\text{O}_3/\text{Pal}$  catalysts are successfully synthesized in this work by a facile sol-gel approach for the photo-SCR of  $\text{NO}_x$  with  $\text{NH}_3$ . Ni-doping shows an obvious influence on NO conversion and selectivity, while the  $\text{LaFe}_{0.5}\text{Ni}_{0.5}\text{O}_3/\text{Pal}$  catalyst demonstrates the best performance reaching as high as 92% of  $\text{NO}_x$  conversion rate in the low temperature range of 150–250 °C.  $\text{H}_2$ -TPR results indicate that the reduction of  $\text{Ni}^{3+}$  to  $\text{Ni}^{2+}$  plays a critical role in the catalytic reduction of  $\text{NO}_x$ . Moreover, with the help of DFT calculation, we find that adequate Ni incorporated into the  $\text{LaFeO}_3$  lattice leads to tune the band gap forming a coherent and staggered heterojunction of  $\text{LaNiO}_3/\text{LaFe}_{1-x}\text{Ni}_x\text{O}_3$ , which results in an enhanced photoresponse and excellent separation of electron-holes under visible light irradiation. This novel catalyst offers a promising fulfilment of the greater need of industrial denitration.

#### Acknowledgments

This work was supported by the National Science Foundation of China (51674043, 51702026), Jiangsu Key Laboratory of Advanced Catalytic Materials and Technology (BM2012110), Priority Academic

Program Development of Jiangsu Higher Education Institutions (PAPD), Jiangsu Technology Support Program (BE2015103, BE2016654) and Social Development Fund of Changzhou City (CE20165022)

#### Appendix A. Supplementary data

Supplementary material related to this article can be found, in the online version, at doi:<https://doi.org/10.1016/j.apcatb.2018.03.008>.

#### References

- [1] K. Skalska, J.S. Miller, S. Ledakowicz, *Sci. Total. Environ.* 408 (2010) 3976–3989.
- [2] S. Roy, M.S. Hegde, G. Madras, *Appl. Energy* 86 (2009) 2283–2297.
- [3] S. Devahashin, C. Fan Jr., K. Li, D.H. Chen, *J. Photochem. Photobiol. A* 156 (2003) 161–170.
- [4] Y.-C. Chou, Y. Ku, *Chem. Eng. J.* 162 (2010) 696–701.
- [5] Y. Qiu, B. Liu, J. Du, Q. Tang, Z. Liu, R. Liu, C. Tao, *Chem. Eng. J.* 294 (2016) 264–272.
- [6] L. Castoldi, R. Matarrese, L. Lietti, P. Forzatti, *Appl. Catal. B-Environ.* 64 (2006) 25–34.
- [7] B. Shen, F. Wang, B. Zhao, Y. Li, Y. Wang, *J. Ind. Eng. Chem.* 33 (2016) 262–269.
- [8] H. Xu, Z. Qu, C. Zong, F. Quan, J. Mei, N. Yan, *Appl. Catal. B-Environ.* 186 (2016) 30–40.
- [9] R. Zhang, W. Yang, N. Luo, P. Li, Z. Lei, B. Chen, *Appl. Catal. B-Environ.* 146 (2014) 94–104.
- [10] Y. Luo, X. Wang, Q. Qian, Q. Chen, *Int. J. Hydrogen Energy* 39 (2014) 15836–15843.
- [11] K. Teramura, T. Tanaka, S. Yamazoe, K. Arakaki, T. Funabiki, *Appl. Catal. B* 53 (2004) 29–36.
- [12] J. Lasek, Y.-H. Yu, J.C.S. Wu, *J. Photochem. Photobiol. C* 14 (2013) 29–52.
- [13] S. Thirumalairajan, K. Girija, N.Y. Hebalkar, D. Mangalaraj, C. Viswanathan, N. Ponpandian, *RSC Adv.* 3 (2013) 7549–7561.
- [14] Y. Qu, W. Zhou, Z. Ren, S. Du, X. Meng, G. Tian, K. Pan, G. Wang, H. Fu, *J. Mater. Chem.* 22 (2012) 16471–16476.
- [15] P. Tang, H. Chen, F. Cao, G. Pan, *Catal. Sci. Technol.* 1 (2011) 1145–1148.
- [16] S. Royer, D. Duprez, F. Can, X. Courtois, C. Batiot-Dupeyrat, S. Laassiri, H. Alamdari, *Chem. Rev.* 114 (2014) 10292–10368.
- [17] J.H. Lee, K.H. Reddy, J.S. Jung, E.-H. Yang, D.J. Moon, *Appl. Catal. A-Gen.* 480 (2014) 128–133.
- [18] Q. Wu, P. Wang, F. Niu, C. Huang, Y. Li, W. Yao, *Appl. Surf. Sci.* 378 (2016) 552–563.
- [19] S. Sun, S. Li, S. Wang, Y. Li, L. Han, H. Kong, P. Wang, *Mater. Lett.* 182 (2016) 23–26.
- [20] C.K. Song, J. Baek, T.Y. Kim, S. Yu, J.W. Han, J. Yi, *Appl. Catal. B-Environ.* 198 (2016) 91–99.
- [21] H. Guo, H. Zhang, F. Peng, H. Yang, L. Xiong, C. Wang, C. Huang, X. Chen, L. Ma, *Appl. Catal. A-Gen.* 503 (2015) 51–61.
- [22] X. Li, C. Ni, C. Yao, Z. Chen, *Appl. Catal. B-Environ.* 117–118 (2012) 118–124.
- [23] X. Li, Z. Zhang, C. Yao, X. Lu, X. Zhao, C. Ni, *Appl. Surf. Sci.* 364 (2016) 589–596.
- [24] X. Li, Y. Yin, C. Yao, S. Zuo, X. Lu, S. Luo, C. Ni, *Particuology* 26 (2016) 66–72.
- [25] X. Li, W. Zhu, X. Yan, X. Lu, C. Yao, C. Ni, *Appl. Phys. A-Mater.* 122 (2016) 1–5.
- [26] S. Luo, W. Zhou, A. Xie, X.Z. Li, C. Yao, *Chem. Eng. J.* 286 (2016) 291–299.
- [27] T. Yu, M. Xu, Y. Huang, *Appl. Catal. B-Environ.* 204 (2017) 525–536.
- [28] T. Zhang, F. Qiu, J. Li, *Appl. Catal. B-Environ.* 195 (2016) 48–58.
- [29] P. Ciambelli, S. Cimino, L. Lisi, M. Faticanti, G. Minelli, I. Pettiti, P. Porta, *Appl. Catal. B-Environ.* 33 (2001) 193–203.
- [30] W.-Y. Lee, H.J. Yun, J.-W. Yoon, *J. Alloys Compd.* 583 (2014) 320–324.
- [31] M. Hepting, D. Kukuruznyak, E. Benckiser, M. Le Tacon, B. Keimer, *Phys. B* 460 (2015) 196–198.
- [32] J.-W. Yoon, E. Di Bartolomeo, E. Traversa, *J. Electroceram.* 26 (2011) 28–31.
- [33] H. Su, L. Jing, K. Shi, C. Yao, H. Fu, *J. Nanopart. Res.* 12 (2010) 967–974.
- [34] K. Zhao, W. Han, G. Lu, J. Lu, Z. Tang, X. Zhen, *Appl. Surf. Sci.* 379 (2016) 316–322.
- [35] I. Ilisz, Z. László, A. Dombi, *Appl. Catal. A-Gen.* 180 (1999) 25–33.
- [36] Q. Zhang, L. Xu, P. Ning, J. Gu, Q. Guan, *Appl. Surf. Sci.* 317 (2014) 955–961.
- [37] S. Royer, D. Duprez, F. Can, X. Courtois, C. Batiot-Dupeyrat, S. Laassiri, H. Alamdari, *Chem. Rev.* 114 (2014) 10292–10368.
- [38] S.M.D. Lima, J.M. Assaf, *Mater. Res.* 5 (2002) 329–335.
- [39] T.A. Westrich, K.A. Dahlberg, M. Kaviani, J.W. Schwank, *J. Phys. Chem. C* 115 (2011) 16537–16543.
- [40] X.Z. Li, X.Y. Yan, S.X. Zuo, X.W. Lu, S.P. Luo, Z.Y. Li, C. Yao, C.Y. Ni, *Chem. Eng. J.* 320 (2017) 211–221.
- [41] T.S. Wang, C.Y. Ni, A. Janotti, *Phys. Rev. B* 95 (205205) (2017) 20–26.
- [42] Y. Wang, H.P. Cheng, *J. Phys. Chem. C* 117 (2013) 2106–2112.
- [43] X.Z. Li, X.Y. Yan, X.W. Lu, S.X. Zuo, Z.Y. Li, C. Yao, C.Y. Ni, *J. Catal.* 357 (2018) 59–68.
- [44] A. Yamamoto, K. Teramura, T. Tanaka, *Chem. Rec.* 16 (2016) 2268–2277.